

# Tunable and Responsive Structural Color from Polymeric Microstructured Surfaces Enabled by Interference of Totally Internally Reflected Light

Amy E. Goodling, Sara Nagelberg, Mathias Kolle, and Lauren D. Zarzar\*

Cite This: *ACS Materials Lett.* 2020, 2, 754–763

Read Online

ACCESS |



Metrics &amp; More

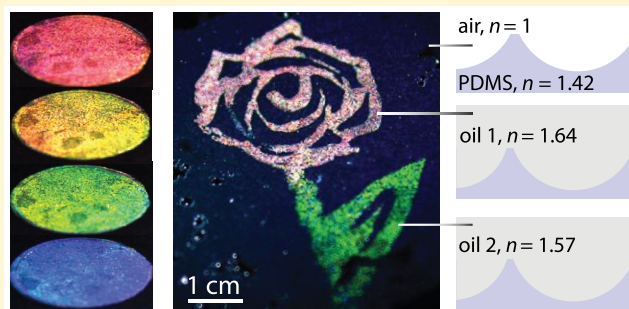


Article Recommendations



Supporting Information

**ABSTRACT:** This report describes a straightforward and versatile approach to the fabrication of polymer films composed of microscale dome or well features that create structural color by interference from total internal reflection. The fabrication approach utilizes assembly of glass particles at monomer oil–water interfaces, providing control over the radius of curvature and contact angle of the resultant microstructures. The influence of the microscale concave interface geometry and refractive index contrast on the structural colors produced is systematically investigated, and the results are compared with those predicted by optical modeling. By dynamically changing such parameters, for example, by deforming the surfaces with mechanical force or using temperature to change refractive index, stimuli-responsive color-changing surfaces and structurally colored patterned images are demonstrated. This simple design and fabrication method to produce structurally colored surfaces may be of interest for both fundamental and applied research areas such as dynamic displays, anticounterfeiting technology, and colorimetric sensors.



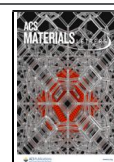
Unlike the color generated from dyes and pigments due to optical absorption,<sup>1</sup> structural colors can be created by optical interference occurring when light interacts with physical structures within or on the surface of a material.<sup>2–4</sup> Recently, we reported that structural coloration is produced when light undergoes multiple total internal reflections (TIRs) at concave microscale interfaces;<sup>5</sup> light rays propagating by different trajectories of TIR along an interface experience varying optical path lengths and a phase shift that leads to interference and structural colors. Unlike well-known nanoscale periodic materials that generate structural color, such as photonic crystals, thin film multilayers, or diffraction gratings,<sup>2,6,7</sup> interference from TIR is due to light interacting with microstructures that have dimensions orders of magnitude larger than the wavelength of visible light.<sup>5</sup> The fundamentally different geometric requirements provide opportunities for controlling structural colors in materials and via processing methods where it previously would not have been possible, such as in liquid droplets as previously reported.<sup>5</sup> Here, we describe a simple route to fabrication of polymeric microwell and microdome-array surfaces that display structural color via TIR interference and characterize how the structural colors are

affected by parameters such as refractive index contrast and microstructure geometry. By assembling commercially available monodisperse glass microparticles at monomer oil–water interfaces and polymerizing the monomer, we create microdome arrays of controllable contact angle and radius of curvature over centimeter scale areas. The microstructured surfaces can be replicated via soft lithography<sup>8</sup> into a range of polymeric materials of varying refractive indices and mechanical properties as a means to tune the structural color and responsivity. We examine in detail the iridescent spectral characteristics of the microdome and microwell arrays as a function of diameter, contact angle, and refractive indices. We also demonstrate tunable color in response to stimuli such as temperature and mechanical deformation. The ability to

Received: April 8, 2020

Accepted: May 27, 2020

Published: May 27, 2020



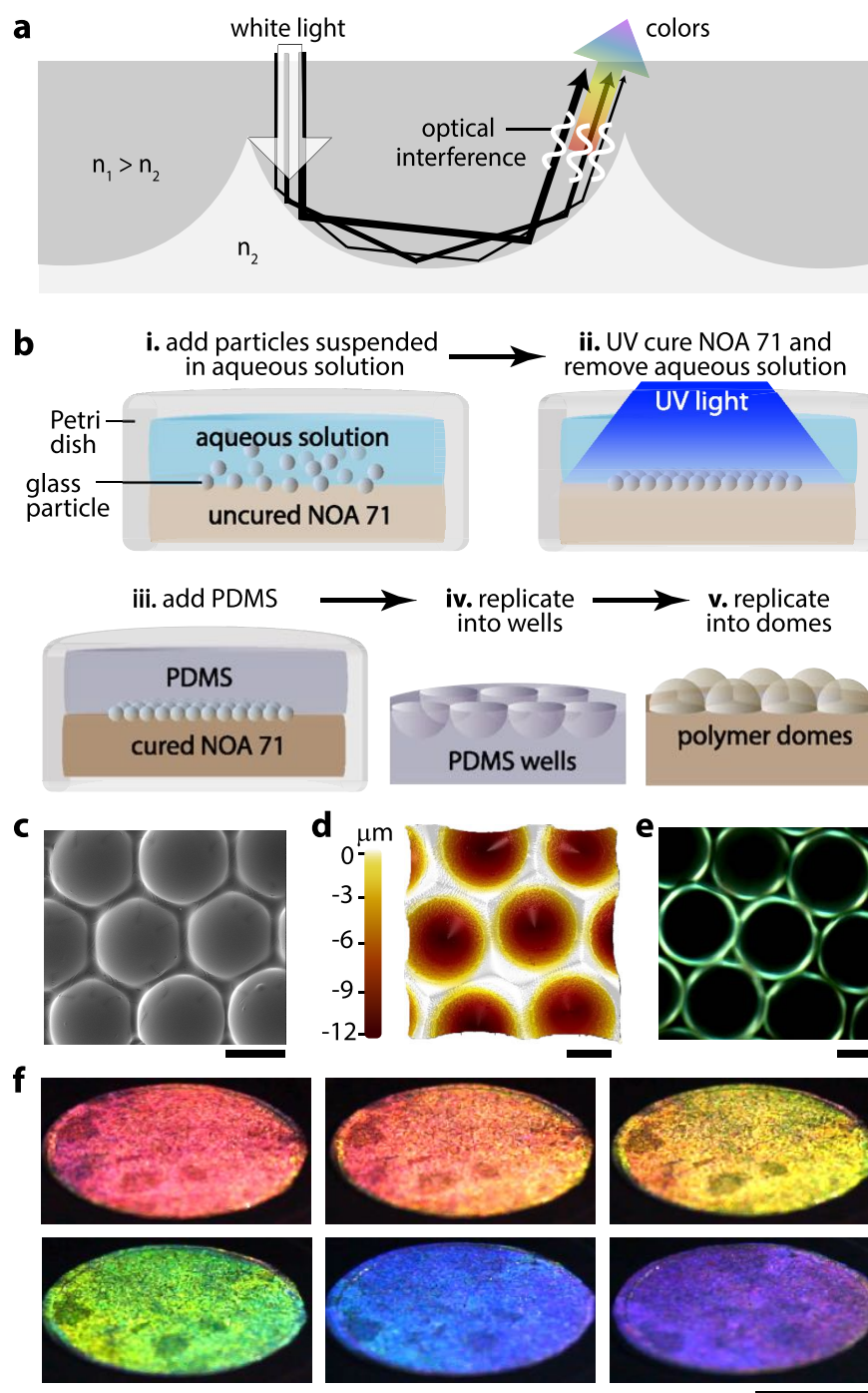


**Figure 1.** Fabrication of microwells and domes with structural coloration due to interference from TIR. (a) Schematic of a concave geometry generating interference from TIR of incident light. Collimated light impinges upon the concave interface between a high and a low index medium and undergoes TIR. Different paths of TIR have different optical path lengths leading to a shift in phase that causes interference and structural color. (b) Method of fabrication for monodisperse microwells and domes. (i) A thin layer of uncured NOA 71 monomer is pipetted into a Petri dish. An aqueous surfactant solution containing monodisperse glass particles is added. The glass particles assemble at the water-NOA 71 interface. (ii) The sample is cured with UV light, leaving the particles embedded partially in the NOA 71. (iii, iv) The surface is molded in crosslinked PDMS to form wells. (v) Polymer domes are replicated from the PDMS wells. See the [Experimental Methods](#) for experimental details. (c, d) Scanning electron microscopy (SEM) and optical profilometry images, respectively, of PDMS wells formed from soda lime glass particles (95% of particles having diameters in the range 40–43  $\mu\text{m}$ ) embedded in NOA 71 deposited from an aqueous solution of 1 mM CTAB and 20% v/v isopropyl alcohol. The resultant wells have  $r = 20.7 \pm 1.1 \mu\text{m}$ ,  $\theta_{\text{CA}} = 76.0 \pm 5.7^\circ$  (average and standard deviation as measured by the optical profilometry, sample size is 45 for radius and 15 for contact angle calculations, respectively). Scale, 25  $\mu\text{m}$ . (e) Reflection optical micrograph of epoxy domes ( $n = 1.51$ ) replicated from PDMS wells with the same geometry as in parts c and d submerged in heptane ( $n = 1.39$ ). Scale, 25  $\mu\text{m}$ . (f) Photographs of the same sample as in part e of epoxy domes ( $n = 1.51$ ) submerged in heptane ( $n = 1.39$ ), viewed macroscopically under collimated white light illumination. As the viewing angle  $\varphi$  rotates, the color changes (as also seen in [Video S1](#)). Scale, 1 cm.

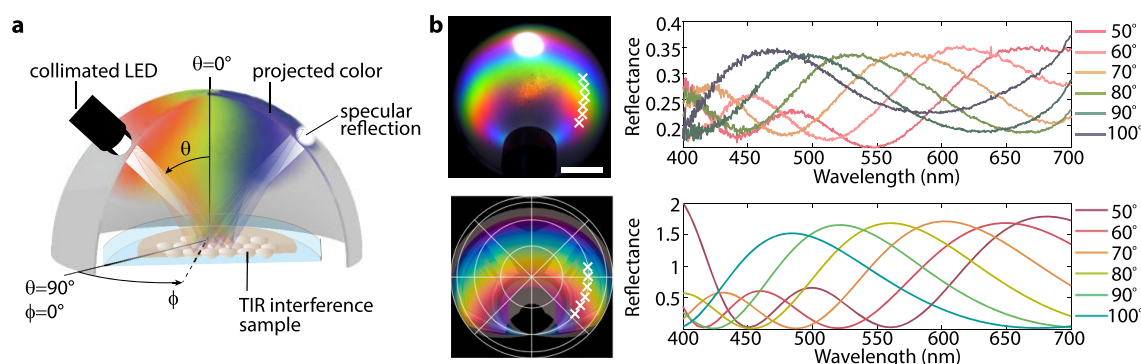


**Figure 2.** Spectral characterization of surfaces generating structural color from TIR. (a) Schematic of the method used to characterize the iridescent color distribution in spherical coordinates. Collimated white LED light illuminates the sample through a 3 mm hole in a translucent hemisphere (a half ping-pong ball). The reflected colors are projected onto the inside surface of the translucent hemisphere, which acts as a screen. The angles of  $\theta$  and  $\varphi$  are defined such that  $\theta = 0^\circ$  corresponds to the sample normal, and the light source is at  $\varphi = 0^\circ$ . (b) Top row: photograph of the reflected color distribution collected as shown in part a from domes of epoxy ( $r = 19.4 \pm 2.0 \mu\text{m}$ ,  $\theta_{CA} = 72.5 \pm 5.1^\circ$ ,  $n = 1.51$ ) backed in water ( $n = 1.33$ ) with corresponding spectra collected at  $\theta = 45^\circ$  for varying values of  $\varphi$ , as color coded in the key. White X in the photograph show where the spectra were collected. Illumination angle was ( $\theta = 45^\circ$ ,  $\varphi = 0^\circ$ ). Scale, 1 cm. Bottom row: modelled color distribution and calculated spectra for domes of ( $r = 18 \mu\text{m}$ ,  $\theta_{CA} = 75^\circ$ ,  $n = 1.505$ ) backed with index  $n = 1.33$  for comparison to the experimental data. The values of the reflectance shown here are estimates relative to a Lambertian scatterer, and a description of the estimation method is included in the [Experimental Methods](#) sections [Measuring the Samples' Reflection Spectra](#) and [Quantifying Reflectance in the Theoretical Model of the Microstructures' Optical Properties](#).

readily harness the TIR interference optical mechanism in polymeric solid films and elastomers may provide accessible routes for utilizing dynamic structural coloration in stimuli-responsive materials, displays, coatings, or sensors.<sup>9–12</sup>

In order to create surfaces with microscale hemispherical structures that support multiple trajectories of TIR to generate interference (Figure 1a), we anticipated that a simple approach for large-area patterning could be partially embedding monodisperse spherical particles at a uniform depth within a polymer film. Our fabrication method is outlined in Figure 1b. In brief, a thin layer of uncured Norland Optical Adhesive 71 (NOA 71) was poured into a Petri dish followed by an aqueous suspension of soda lime glass particles (40–43  $\mu\text{m}$  diameter with 95% of particles in range, 0.01 g/mL) in 1 mM hexadecyltrimethylammonium bromide (CTAB) aqueous surfactant. The CTAB was necessary to render the particles sufficiently hydrophobic to be wetted by the NOA 71 and partially sink into the oil–water interface. UV light exposure was used to cure the NOA 71 and fix the particles in place. We then washed away the aqueous phase, leaving behind an array of glass spheres partially embedded in polymer. An inverse replica of this domed surface was fabricated in crosslinked polydimethylsiloxane elastomer (PDMS) to form a uniform array of wells (Figure 1c,d). The PDMS wells could be subsequently used as a mold to fabricate polymer domes of various materials, such as UV-curable polymers, numerous times via soft lithography.<sup>8</sup> Domes replicated in epoxy OG142-87 ( $n = 1.51$ ) when viewed in air ( $n = 1$ ) appeared white in reflection (Figure S1). The air backing creates a large refractive index contrast resulting in many trajectories of TIR which do not all interfere constructively resulting in muter colors; increased refractive index contrast also results in a larger amount of background reflection which further washes out the colors, thereby causing a white appearance. However, when the epoxy surface was submerged in heptane ( $n = 1.39$ ) to reduce the refractive index contrast, bright structural coloration was observed (Figure 1e,f, Video S1).

Because these iridescent surfaces display different colors as a function of viewing and illumination angle, we required a

method to “map” the iridescence in three dimensions in order to characterize and compare the optical properties of the surfaces. We used our previously reported method<sup>5</sup> in which the sample’s reflected light is “projected” onto the inside of a translucent hemispherical screen (which is a half of a ping-pong ball), providing correlation of the colors with specific reflection directions in spherical coordinates (Figure 2a). Qualitative comparison of an experimentally collected color distribution from the sample shown in Figure 1e,f with a simulated color distribution<sup>5</sup> for the same geometry, refractive indices, and illumination angle yielded a close match (Figure 2b). We used a spectrometer to collect a reflection spectrum for several specific reflection angles and found that the spectra also matched well with those predicted by the interference optical model (Figure 2b).<sup>5</sup> Please refer to the [Experimental Methods](#) section for information on the optical model. Thus, this fabrication method appeared suitable for the formation of microwell or microdome arrays that, upon interfacing with an appropriately high or low refractive index material, respectively, can generate bright iridescent color from TIR interference.

Having developed a straightforward method to fabricate polymer surfaces displaying TIR interference, we next investigated whether we could control the structural color through variations in geometrical parameters and refractive index contrast. Based on the mechanism of TIR interference,<sup>5</sup> we expect the structural colors to be dependent on the contact angle and radius of curvature of the concave optical interface. For a given glass microparticle used during surface fabrication, the contact angle,  $\theta_{CA}$ , of the resultant dome should be dependent on the contact angle of the microparticle at the monomer oil–water interface (e.g. how far the particle sinks into the monomer oil). Particles that are more deeply embedded into the monomer would thus result in domes with a lower effective contact angle (and hence, shallower wells upon replication in PDMS, following the procedure in Figure 1b). We found that, by varying the concentration of isopropyl alcohol in the aqueous CTAB solution, we were able to tune the interfacial tension and manipulate how far the glass

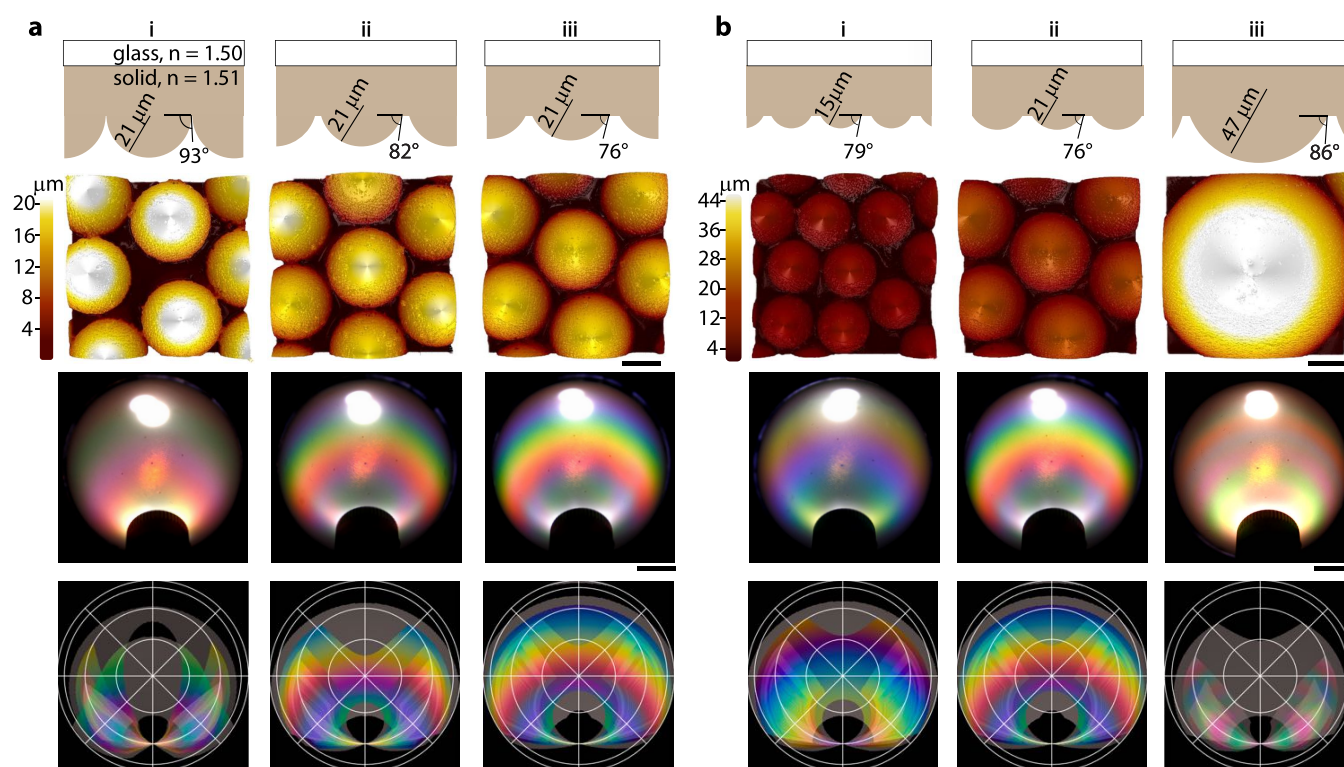


**Figure 3.** Contact angle and radius of curvature of the microwells and domes affect the structural color. (a) The contact angle of the microdomes was tuned by using varying concentrations of isopropyl alcohol during initial assembly of particles (following the procedure in [Figure 1](#)). Top row: resultant geometries of structures replicated from PDMS molds of 40–43  $\mu\text{m}$  diameter particles embedded in NOA 71 from (i) 0% v/v, (ii) 10% v/v, and (iii) 20% v/v isopropyl alcohol with 1 mM CTAB. These conditions yielded  $r = 20.7 \pm 1.1 \mu\text{m}$  and  $\theta_{\text{CA}} = 93 \pm 5.1^\circ$ ,  $82 \pm 5.4^\circ$ , and  $76.0 \pm 5.7^\circ$  for geometries i–iii, respectively. The radius of curvature and contact angles were measured using optical profilometry (second row, scale is 20  $\mu\text{m}$ ). Third row: photographs of the color distribution generated from replica epoxy domes ( $n = 1.51$ ) submerged in water ( $n = 1.33$ ) for geometries i–iii. Light angle ( $\theta = 45^\circ$ ,  $\varphi = 0^\circ$ ), camera angle ( $\theta = 0^\circ$ ,  $\varphi = 0^\circ$ ). Scale, 1 cm. Bottom row: calculated color distributions. Input parameters for model values:  $r = 20.0 \mu\text{m}$  and  $\theta_{\text{CA}} = 95.0^\circ$ ,  $80.0^\circ$ , and  $76.0^\circ$ . (b) Varying the diameter of monodisperse glass particles used during fabrication (following method from [Figure 1](#)) was used to tune the radius of curvature of the resultant microwells and domes. Specifically, the samples shown are epoxy dome replicas fabricated from PDMS molds of particles of (i) 29–32, (ii) 40–43, and (iii) 98–102  $\mu\text{m}$  diameter deposited from aqueous surfactant solution of 1 mM CTAB and 20% v/v isopropyl alcohol. These conditions yielded geometries of ( $r = 14.6 \pm 0.8 \mu\text{m}$ ,  $\theta_{\text{CA}} = 79.2 \pm 3.9^\circ$ ) for i, ( $r = 20.7 \pm 1.1 \mu\text{m}$ ,  $\theta_{\text{CA}} = 76.1 \pm 5.7^\circ$ ) for ii, and ( $r = 47.0 \pm 6.4 \mu\text{m}$ ,  $\theta_{\text{CA}} = 86.4 \pm 4.6^\circ$ ) for iii. Stated dimensions are the averages and standard deviations as measured by optical profilometry (second row, scale 20  $\mu\text{m}$ ). Third and fourth rows are photographs of the color distributions and calculated color distributions, respectively, correlating to the dimensions of part b, i–iii (scale, 1 cm). Input parameters for the calculated color distributions: ( $r = 14.0 \mu\text{m}$ ,  $\theta_{\text{CA}} = 79.0^\circ$ ) for i, ( $r = 20.0 \mu\text{m}$ ,  $\theta_{\text{CA}} = 76.0^\circ$ ) for ii, and ( $r = 50.0 \mu\text{m}$ ,  $\theta_{\text{CA}} = 85.0^\circ$ ) for iii.

particles penetrated into the oil layer for  $\theta_{\text{CA}}$  values ranging from  $76.0 \pm 5.7^\circ$  to  $93.2 \pm 5.1^\circ$  (average and standard deviation determined by optical profilometry, sample sizes of at least 14 structures). In order to expand the range of accessible contact angles, we replaced the aqueous CTAB surfactant solution during surface fabrication with PDMS oil of varying viscosity, which we anticipated would alter the wetting dynamics of the particles at the liquid–liquid interface.<sup>13,14</sup> Use of PDMS oil with viscosity of 10 cSt resulted in a contact angle of  $75.4 \pm 1.8^\circ$ , close to that produced using an aqueous phase with CTAB and 20 wt % isopropanol solution; when 1 cSt viscosity PDMS oil was instead used, much lower contact angles of  $52.3 \pm 2.6^\circ$  were generated ([Figure S2](#)). Particles that were embedded at a contact angle much higher than  $\theta_{\text{CA}} = 90^\circ$  could not be easily replicated by PDMS molding and thus were not considered here.

Domes with contact angles ranging from  $\approx 76^\circ$  to  $93^\circ$  made of a UV-curable epoxy OG 142-87 ( $n = 1.51$ ) were submerged in water ( $n = 1.33$ ), and their color distributions were collected at an illumination angle of ( $\theta = 45^\circ$ ,  $\varphi = 0^\circ$ ) ([Figure 3a](#)). The contact angle of the domes determined which light trajectories

were allowed for a given input and output angle combination; as the contact angle decreased from  $93^\circ$  to  $76^\circ$ , the total number of light rays that were able to undergo TIR upon impinging at the concave interface increased for the given illumination angle, and hence the number of possible trajectories of TIR was also increased. As a result, more vibrant and distinct colors were seen in [Figure 3a,iii](#) (lower contact angle) as compared to [Figure 3a,i](#) (higher contact angle). The experimental color distributions matched well with the calculated color distributions ([Figure 3a](#), [Figure S3](#)).

The radius of curvature,  $r$ , is also expected to influence the structural color because it impacts the optical path length for light undergoing TIR. Radius of curvature is most easily manipulated by starting with glass particles of a different diameter upon initial surface fabrication. We examined surfaces generated from three diameters of particles (29–32, 40–43, and 98–102  $\mu\text{m}$ , 95% of particles falling in range). Resultant PDMS wells (and subsequent replicated domes) had average  $r$  with standard deviation of  $14.6 \pm 0.8$ ,  $20.7 \pm 1.1$ , and  $47.0 \pm 6.4 \mu\text{m}$ , respectively, as determined by optical profilometry for sample sizes of 76, 45, and 10, respectively ([Figure 3b](#)).

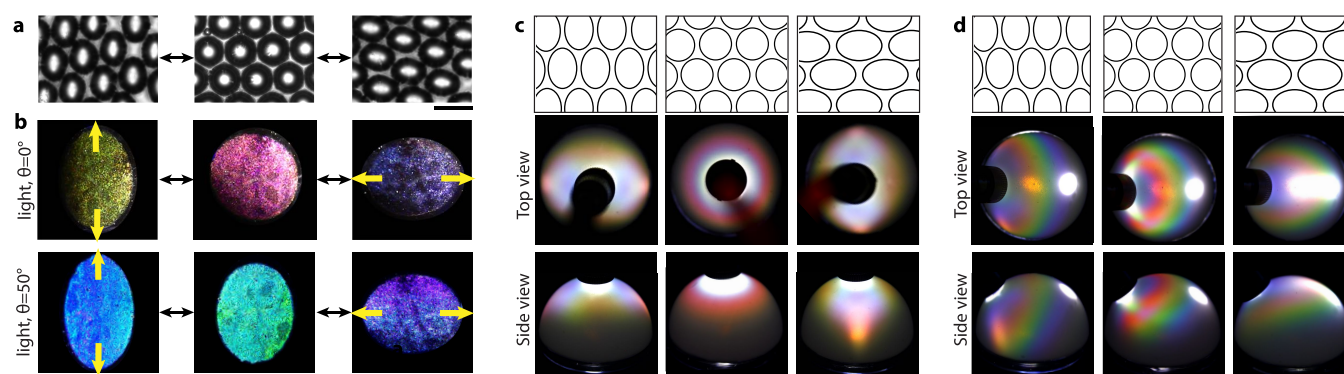


**Figure 4.** Mechanical deformation was used to create ellipsoidal wells and domes and alter structural color. (a) Transmission optical micrographs of wells that have been stretched in two different directions, which correspond to the macroscale images aligned beneath in part b. Scale, 50  $\mu\text{m}$ . (b) Photographs of elastomeric PDMS wells ( $n = 1.42$ ) with the same geometry as part a, ( $r = 20.7 \pm 1.1 \mu\text{m}$ ,  $\theta_{\text{CA}} = 76.0 \pm 5.7^\circ$ ) filled with a high index UV-curable elastomer ( $n = 1.53$ ) being stretched and viewed under two different illumination and viewing conditions. Top row illumination ( $\theta = 0^\circ$ ,  $\varphi = 0^\circ$ ) and camera ( $\theta = 15^\circ$ ,  $\varphi = 90^\circ$ ); bottom row illumination ( $\theta = 50^\circ$ ,  $\varphi = 0^\circ$ ) and camera ( $\theta = 50^\circ$ ,  $\varphi = 110^\circ$ ). The three images in each row correspond to the unstretched sample (middle) and stretching in two orthogonal directions (left and right). Yellow arrows show the stretching direction relative to the unstretched sample (center). Scale, 1 cm. (c, d) Photographs of the projected color distributions from ellipsoidal domes with geometry similar to parts a and b but replicated in epoxy ( $n = 1.51$ ) and submerged in water ( $n = 1.33$ ). Schematics in the top row illustrate the surface orientation of the ellipsoidal domes. Images in part c were taken under illumination at ( $\theta = 0^\circ$ ,  $\varphi = 0^\circ$ ), and images in part d were taken under illumination at ( $\theta = 50^\circ$ ,  $\varphi = 0^\circ$ ). In part d, the major axis of the ellipsoids is at  $\varphi = 90^\circ$  (leftmost image) and  $\varphi = 0^\circ$  (rightmost image) defined relative to the light, as shown in the top-row schematics. Scale, 1 cm.

Structural color distributions from domes fabricated in epoxy OG 142-87 ( $n = 1.51$ ) and submerged in water ( $n = 1.33$ ) of the three differently sized domes are shown in Figure 3b and compared well with the colors predicted by the optical model. For a constant refractive index contrast, the dome array with the smallest  $r$  had the largest angular separation of the colors, while larger values of  $r$  generated bands of color that were narrower and more closely spaced. In essence, for domes with smaller radii, each ray trajectory is shorter, and the optical path length difference between interfering paths is smaller, resulting in less pronounced spectral shifts as a function of viewing angle.

Having developed a method to fabricate the structurally colored surfaces in elastomeric PDMS, we were interested as to whether mechanical deformation could be used to actuate the colors and examine the effect of an anisotropic structure on the resultant iridescence. We created PDMS wells ( $n = 1.42$ ,  $r = 20.7 \pm 1.1 \mu\text{m}$ ,  $\theta_{\text{CA}} = 76 \pm 5.0^\circ$ ) filled with a higher refractive index silicone, Dowsil VE-6001 ( $n = 1.53$ ), to produce a fully solidified elastomeric sample. Stretching of the elastomer wells by even 10% or 15% resulted in significant mechanically induced shifts in structural color (Figure 4a,b, Video S2). To create surfaces with an array of permanent ellipsoidal structures, PDMS wells were filled with UV-curable epoxy OG 142-87 ( $n = 1.51$ ), which was polymerized while strain in the PDMS was maintained at 15%. The anisotropic ellipsoidal domes, along with precursor spherical domes of the same material, were then submerged in water ( $n = 1.33$ ), and color distribution maps were collected at illumination angles of ( $\theta = 0^\circ$ ,  $\varphi = 0^\circ$ ) and ( $\theta = 50^\circ$ ,  $\varphi = 0^\circ$ ) for ellipsoidal major axis orientations along  $\varphi = 0^\circ$  and  $90^\circ$  (Figure 4c,d). Under illumination at ( $\theta = 0^\circ$ ,  $\varphi = 0^\circ$ ) the spherical domes generated a circularly symmetric color distribution with a singular ring of color, largely red, centered around the light source (Figure 4c, middle column). In comparison, ellipsoidal structures under the same illumination had a distinctly different color distribution, where the red nearly entirely disappeared and was replaced by a light blue and green oval pattern with the

long axis of the oval perpendicular to the long axis of the ellipsoidal domes (Figure 4c). The elliptical domes imaged with an oblique light angle ( $\theta = 50^\circ$ ,  $\varphi = 0^\circ$ ) similarly yielded a “stretched” version of the color distribution pattern as compared to the spherical domes (Figure 4d). Hence, the surfaces’ colors can be varied by mechanical deformation of an elastomeric surface or rotation of ellipsoidal structures, not only changing the positions of colors but in some cases actually generating new colors previously not visible under the given illumination conditions.

In addition to geometric effects influencing structural color from TIR, we also expect refractive index contrast to impact the reflected color distribution, because the critical angle for TIR,  $\theta_c$ , is directly related to the refractive indices at the optical interface, where  $\theta_c = \arcsin(n_2/n_1)$ .<sup>15</sup> As the refractive index contrast increases, the critical angle decreases, and more paths of TIR become available. To examine the effect of the refractive index contrast on the structural color, we filled PDMS wells ( $n_2 = 1.42$ ) with liquids of varying refractive index, where the refractive index was tuned through mixing of tetrabromoethane ( $n_1 = 1.64$ ), benzyl benzoate ( $n_1 = 1.57$ ), and  $n$ -decane ( $n_1 = 1.41$ ). The color distributions were collected at an illumination angle of ( $\theta = 50^\circ$ ,  $\varphi = 0^\circ$ ) for several refractive index contrasts (Figure 5a). At too low of an index contrast (e.g.,  $n_1 = 1.49$ , in Figure 5a), an insignificant fraction of light undergoes TIR, and no reflected colors were observed. As the refractive index contrast increased, more paths of TIR became available, leading to interference and causing bands of color to appear. Use of increasingly higher refractive index oils affected the perceived color in multiple ways. Besides increasing the refractive index contrast, and thus increasing the total amount of light undergoing TIR, increasing  $n_1$  also refracts the illuminating light rays to a greater degree such that the illuminating rays have slightly different incident angles upon striking the concave microscale interface; this refraction may not only contribute to increased availability of TIR paths but may also produce a slight shift in the position of

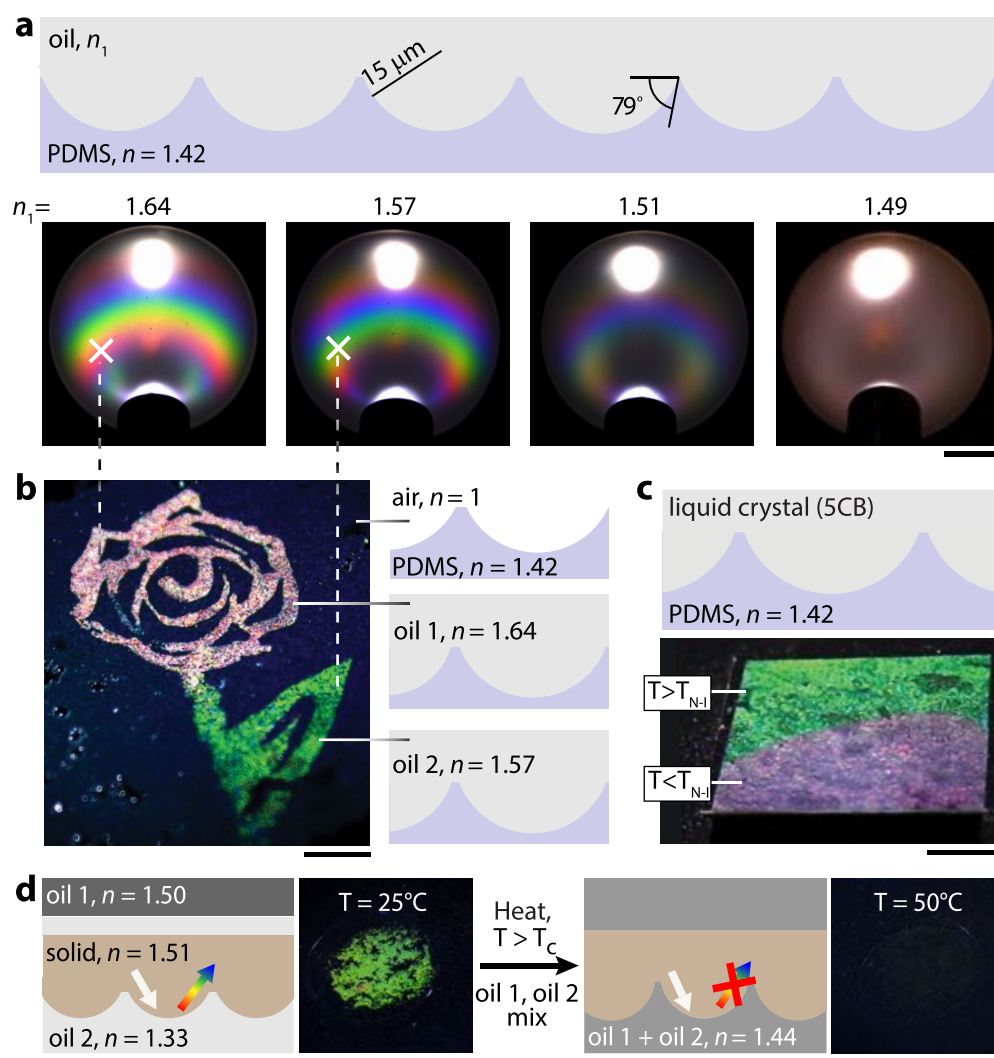


**Figure 5.** Patterned and responsive structural color patterns achieved by varying refractive index contrast. (a) To probe the effect of refractive index contrast on the structural color, we filled PDMS wells ( $r = 14.6 \pm 0.8 \mu\text{m}$ ,  $\theta_{\text{CA}} = 79.2 \pm 3.9^\circ$ ) with oils of increasingly lower refractive index. Different oil refractive indices were achieved through mixing of tetrabromoethane ( $n = 1.64$ ), benzyl benzoate ( $n = 1.57$ ), and/or *n*-decane ( $n = 1.42$ ). As the refractive index contrast was reduced, the color began to fade as less light undergoes TIR. Scale, 1 cm. (b) PDMS wells from part a were filled with different refractive index oils (benzyl benzoate,  $n = 1.57$ , and tetrabromoethane,  $n = 1.64$ ), to create a structurally colored image of a rose. Camera, ( $\theta = 50^\circ$ ,  $\varphi = 40^\circ$ ); illumination, ( $\theta = 50^\circ$ ,  $\varphi = 0^\circ$ ). Scale, 1 cm. (c) Temperature-responsive color change achieved by filling PDMS wells (same geometry as used in part a) with 5CB liquid crystal. At room temperature, the nematic 5CB anchored on the surface of the PDMS (Figure S5) and the birefringence affected interference from TIR resulting in less colorful, pinkish hues. As the sample was heated, the 5CB underwent a nematic to isotropic transition, losing molecular alignment, and coloration from TIR interference became more intense. Scale, 5 mm. (d) Iridescent color switched on and off in response to temperature by varying the index contrast at the optical interface through oil mixing. Domes of epoxy ( $n = 1.51$ ) with the same geometry as in part a were immersed in low index 2-(trifluoromethyl)-3-ethoxydodecafluorohexane (oil 2,  $n = 1.33$ , refractive index measured after saturating with the hydrocarbon mixture) onto which an immiscible layer of higher index hydrocarbon (5:1 volume ratio of toluene to benzyl benzoate, oil 1,  $n = 1.50$ ) was added. A 3:1 volume ratio of hydrocarbon to fluorocarbon oil was used. The sample and solution were heated above the oils' critical solution temperature ( $T_c < T = 50^\circ\text{C}$ ), which led to oil mixing (new refractive index  $n = 1.44$ ). The index contrast with the polymer domes was thus reduced and the color faded. The color change was reversible upon cooling. Scale, 5 mm.

the color bands, as seen in Figure 5a. Increasing  $n_1$  also increases the optical path length of each of the light trajectories; this has an effect similar to increasing the size of the dome and is due to the fact that the optical path length is the product of physical path length and the refractive index. If  $n_1$  is increased while holding the refractive index contrast constant (i.e.,  $n_2$  increased proportionally) then the same change in color would be expected as occurs when changing only the radius of curvature (again, proportionally). The magnitude of refractive index contrast ( $n_1/n_2$ ) also determines

the amount of phase change occurring upon each reflection and so also affects the colors that are observed. Higher index contrast additionally leads to an overall increase in the intensity of the reflected light (Figure 5a); however, if too high of a refractive index contrast is used, the surface appears whiter as a result of the many possible trajectories of TIR which do not all interfere constructively and hence generate muter colors (Figure S1). While the experiments shown in Figure 5a only examine the effect of refractive index  $n_1$  for one specific radius of curvature and contact angle, additional combinations of geometries and index contrasts achieved by

varying  $n_2$  are shown in Figure S4. In summary, changing the refractive index contrast allows tuning of the intensity and direction of the reflected colors due to variations in refraction and changes to TIR trajectories and path length differences that cause the interference.

We used the variation in color as a function of refractive index contrast to construct an iridescent multicolored image by “painting” onto the PDMS wells with different refractive index oils, benzyl benzoate ( $n = 1.57$ ) and tetrabromoethane ( $n = 1.64$ ) (Figure 5b, Video S3). Glass capillary tubes loaded with each oil were touched to the PDMS wells to selectively fill specific wells with the oil. Wells filled with high index oils generated TIR interference, whereas the empty wells appeared black, because they do not have the appropriate index contrast for TIR (Figure 5b). When illuminated at an angle of ( $\theta = 50^\circ$ ,  $\varphi = 0^\circ$ ) and viewed at ( $\theta = 30^\circ$ ,  $\varphi = 40^\circ$ ), the wells filled with the higher index tetrabromoethane appeared a pastel pink while the wells filled with benzyl benzoate gave a vibrant green color, yielding a picture of a rose. These colors correlated, as expected, to the angular positions in the color distribution maps for those index contrasts (Figure 5a,b). We also explored whether dynamic changes in refractive index contrast could be used to responsively change the reflected color. Liquid crystals experience abrupt changes in birefringence, and hence refractive index, when undergoing transitions between ordered and disordered phases.<sup>16</sup> Curious as to how birefringent liquid crystals would influence interference from TIR, we filled PDMS microwells ( $n = 1.42$ ,  $r = 20.7 \pm 1.1 \mu\text{m}$ ,  $\theta_{\text{CA}} = 76.0 \pm 5.7$ ) with 4-cyano-4'-pentylbiphenyl (5CB) liquid crystal. At room temperature, 5CB has a nematic structure with vertical molecular alignment on PDMS<sup>17</sup> (Figure S5) and refractive indices for the extraordinary and ordinary ray<sup>18</sup> ( $n_e \approx 1.72$ ,  $n_o \approx 1.53$ ) that are high enough, in principle, to produce color through TIR when paired with PDMS wells ( $n = 1.42$ ). However, the birefringence influenced the TIR interference mechanism and resulted in a dull, polarization dependent pinkish reflection. When the sample was heated above the nematic-to-isotropic phase transition temperature ( $T_{\text{N-I}} = 35^\circ\text{C}$ ),<sup>18</sup> the liquid crystal transitioned into an isotropic state with  $n = 1.59$ , and vibrant iridescent colors due to TIR interference became visible (Figure 5c, Video S4). This temperature-induced color change transition was fully reversible. The reflected color could also be thermally switched on and off by backing domes with two immiscible oils that, upon heating above a critical temperature, mix to form a solution that has too low of an index contrast for TIR. This approach is shown in Figure 5d with domes of epoxy ( $n = 1.51$ ) submerged in a low index fluorinated oil, 2-(trifluoromethyl)-3-ethoxydodecafluorohexane (pure oil,  $n = 1.28$ ), with a higher index hydrocarbon oil mixture (benzyl benzoate and toluene in a 1:5 volume ratio,  $n = 1.50$ ) floating on top. The index contrast between the domes and fluorinated oil supports TIR to give an iridescent color, but as the solution was heated above the oils' critical solution temperature ( $T_c < T = 50^\circ\text{C}$ ) all oils became miscible, raising the refractive index of the mixture to  $n = 1.44$ . As shown in Figure 5d, this index contrast was too low to generate TIR interference, and the color disappeared. This mechanism was also fully reversible, and upon cooling below  $T_c$ , the color reappeared.

In summary, we have presented a straightforward method to produce and manipulate structural coloration in polymeric surfaces by harnessing interference from total internal reflection in microwells and microdome structures. The

approach of embedding glass particles at the interface of water or PDMS oil and UV-curable monomer provided a route to tuning both the radius of curvature and contact angle of the resultant hemispherical microstructures, key geometric parameters that affect the structural color. Surfaces fabricated with this method could be easily replicated into other polymers of choice via PDMS molding. We examined the relationship between contact angle, radius of curvature, refractive index contrast, and structure symmetry on the distribution of reflected colors and compared the results to those predicted by optical modeling. By dynamically changing such parameters, for example, by deforming the surfaces with mechanical force or using temperature to change refractive index, we could create stimuli-responsive color-changing surfaces and structurally colored patterned images. Many other stimuli-responsive polymeric platforms with similar geometries could be envisioned, such as those that respond to pH, ionic strength, or biomolecules to create colorimetric sensors,<sup>19–22</sup> for example. Given that long-range nanoscale periodicity is not needed, we expect that this fabrication approach and optical mechanism may provide an accessible route to creating and tuning structural colors over larger areas in a greater diversity of materials than is currently accessible, enabling applications ranging from dynamic camouflage to anticounterfeiting technology.

## EXPERIMENTAL METHODS

**Chemicals and Materials.** Hexadecyltrimethylammonium bromide (CTAB) (Fluka, >99.0%), isopropyl alcohol (VWR, >99.8%), Norland Optical Adhesive 71 (Norland), benzyl benzoate (Alfa Aesar, 99+%), *n*-decane (Alfa Aesar, 99+%), 1,1,2,2-tetrabromoethane (TCI, >98.0%), toluene (VWR, >99.5%), 2-(trifluoromethyl)-3-ethoxydodecafluorohexane (Synquest Laboratories, 99%), perfluorooctane (TMC Industries, >98%), 4-cyano-4'-pentylbiphenyl (Frontier Scientific, 99%), Sylgard 184 polydimethylsiloxane (PDMS) (Dow Corning), Dowsil VE-6001 UV Optical Bonding (Dow Corning), PMS Black Silc Pig pigment (SmoothOn), soda lime glass particles (40–43, 29–32, 98–102  $\mu\text{m}$  diameter, 2.5  $\text{g}/\text{cm}^3$ ) (Cospheric), OG 142-87 epoxy (Epotek), and PDMS oil of 10 cSt and 1 cSt (Gelest) were used.

**Microdome and Microwell Fabrication Method.** Uncured NOA 71 was placed into a thin layer in a Petri dish. An aqueous solution of 1 mM CTAB with 0.01g/mL of dispersed glass particles (40–43, 29–32, or 98–102  $\mu\text{m}$  diameter) was pipetted onto the surface of the uncured NOA 71. The dense particles sank to the water–monomer interface, forming a monolayer. Isopropyl alcohol could be added to the particle solution in varying concentrations (0% v/v, 10% v/v, and 20% v/v) to tune the depth the particles settled at the aqueous–monomer interface. The samples were then cured using an OmniCure UV lamp (mercury bulb, 17  $\text{W}/\text{cm}^2$ ) for 1 min, fixing the particles into the cured optical adhesive. The aqueous phase was then removed, and the sample was washed with water and baked at 50  $^\circ\text{C}$  for 12 h to complete the curing of the NOA 71. A variant of this method was achieved with using PDMS oil (either 1 or 10 cSt) instead of the aqueous phase; the procedure was otherwise the same. Dow Corning Sylgard 184 PDMS was then used to create an inverse replica from the soda lime silica particles fixed in the cured NOA 71. The PDMS base and hardener were mixed in a 10:1 mass ratio, mixed, degassed, poured over the polymer sample, and cured in an oven at 50  $^\circ\text{C}$  for at least 2 h. The cured PDMS was

peeled off the fixed particles to yield an array of wells. The PDMS wells could be used directly to create the structural color by filling the wells with a high refractive index oil or polymer, or the wells could be used as a mold to fabricate domes of various polymers, such as epoxy OG 142-87.

**Sample Imaging and Characterization.** For large-area sample illumination, an Amscope LED-50W light with a collimating lens was used to illuminate the sample. For selected area illumination, a Thorlabs LED light (MWWHF2, 4000 K, 16.3 mW) equipped with a  $\varnothing 200 \mu\text{m}$  fiber optic cable and collimating lens (CFC-2X-A) was used. The translucent dome used for capturing the iridescent color distribution pattern was created by cutting a 40 mm diameter ping-pong ball in half with a razor blade and drilling a 3 mm diameter hole in the side with a Dremel Model 220 device. The ping-pong ball dome screen was then placed on top of the well or dome sample, and collimated light from the LED was passed through the hole into the center of the sample. All macroscale photographs were taken using a Canon EOS Rebel T6 DSLR camera mounted to an optical table and positioned at specific angles, as indicated in the primary text. Scanning electron micrograph (SEM) images were taken using an FEI Nova NanoSEM 630 instrument. Profilometry images were taken using a Zygo NexView 3D Profilometer. Optical microscope bright-field images were taken using a Nikon Eclipse Ti-U inverted microscope and an Image Source DFK 23UX249 color camera.

**Effect of Varying Refractive Index Contrast on Color.** To test how the refractive index affects the perceived color (Figure 5), PDMS wells replicated from 40–43  $\mu\text{m}$  glass particles embedded in NOA 71 originally in an aqueous phase of 1 mM CTAB and 20% v/v in isopropyl alcohol were filled with varying concentrations of tetrabromoethane, benzyl benzoate, and *n*-decane to observe the effect of refractive index difference at the concave interface. The refractive indices of the oil mixtures were measured using a J457FC refractometer (Rudolph Research Analytical).

**Mechanical Force Experiments.** Stretchable films of well arrays were fabricated by removing cured NOA 71 with fixed soda lime silica particles (40–43  $\mu\text{m}$  diameter) at the surface from its 5.5 cm Petri dish and placing it in a larger 8.5 cm Petri dish. PDMS dyed black with Silc pig pigment was then poured over the polymer sample and cured to form an array of microwells that were indented into a 5.5 cm well a couple mm deep. Dowsil VE-6001 was used to fill the 5.5 cm well with the PDMS and cured with an OmniCure UV lamp (mercury bulb, 17 W/cm<sup>2</sup>) for 2 min. Because the Dowsil remains tacky when cured, an additional thin (1 mm) layer of transparent PDMS poured on the surface and cured to form the sample.

**Fabricating Ellipsoidal Domes.** A sample of glass particles (40–43  $\mu\text{m}$  diameter) embedded in NOA 71 was prepared from an aqueous solution of 1 mM CTAB and 20% v/v in isopropyl alcohol. PDMS wells were molded from the embedded particles. These wells were stretched using two metal clamps, filled with uncured OG 142-87, and then UV cured for 1 min at 100% power of an OmniCure UV lamp (mercury bulb, 17 W/cm<sup>2</sup>). The polymerized domes were then removed from the PDMS mold. The cured polymer was then removed and backed with water to give an index contrast that promotes TIR and iridescent color.

**Liquid Crystal Heating.** PDMS wells replicated from particles embedded in NOA 71 originally in an aqueous phase of 1 mM CTAB and 20% v/v in isopropyl alcohol were filled

with 5CB liquid crystal in its nematic state at room temperature. The wells were heated to 40 °C on a hot plate, above the nematic to isotropic transition temperature, where the liquid crystal loses its birefringence, and the resulting color became much more vibrant.

**Drawing Structural Color Images in Microwells.** PDMS wells replicated from particles (29–32  $\mu\text{m}$  diameter) embedded in NOA 71 fabricated using an aqueous phase of 1 mM CTAB and 20% v/v in isopropyl alcohol were selectively filled to create an image. 1.05 mm ID, 1.5 mm OD borosilicate square capillary tubes were filled with benzyl benzoate or tetrabromoethane. The capillary was dragged across the surface of the PDMS, filling the wells with the oils to create an image of a rose.

**Temperature-Responsive Structural Color Using Phase Separation of Oils.** PDMS wells were generated from particles (40–43  $\mu\text{m}$ ) embedded in NOA 71 originally deposited from an aqueous phase of 1 mM CTAB and 20% v/v in isopropyl alcohol. Domes ( $n = 1.51$ ) were replicated from the PDMS wells, and the surface was placed in a 35 mm Petri dish containing fluorinated oil, 2-(trifluoromethyl)-3-ethoxydodecafluorohexane ( $n = 1.33$ ), which gave a refractive index difference that generates coloration from multiple TIR. A 5:1 volume mixture of toluene to benzyl benzoate (final refractive index of  $n = 1.50$ ) was placed on top of the fluorinated oil with the dome array. The hydrocarbon oil mixture and the fluorinated oil were used in a 3:1 volume ratio. At room temperature, the toluene and benzyl benzoate solution are immiscible with the fluorinated phase, but once heated to 35 °C, all the oils became miscible, raising the refractive index of the mixture to  $n = 1.44$ . This high refractive index backing of the domes no longer supported TIR to produce structural color. Upon cooling back to room temperature, the fluids phase separated, and color was again visible.

**Measuring the Samples' Reflection Spectra.** Experimental spectra were collected with an Ocean Optics Maya2000Pro spectrometer. The sample was placed in a water-filled Petri dish on a Thorlabs rotation stage. A collimated optical fiber was mounted at a polar angle of 45°, illuminating the sample with an Ocean Optics halogen light source HL-2000. The spectrometer was coupled into another collimated optical fiber also mounted at 45° on the rotation stage, such that both the sample and spectrometer rotated together. This allowed us to vary the azimuthal angle between the light and collection fibers as the spectra were collected (integration time  $t_{\text{sample}} = 5$  seconds). A mirror was used as a reference (integration time  $t_{\text{mirror}} = 7.2$  ms), and the illumination was turned off in order to collect the background signals  $B_{\text{sample}}$  and  $B_{\text{mirror}}$  for the respective integration times, which were subtracted from the sample and the reference spectra.

In order to estimate the samples' reflectance in relation to a Lambertian scatterer, we estimate the collection solid angle of the collimated fibers to be  $\Omega_c = 0.0012$  sr (4 square degrees). We also assume that the collected intensity scales linearly with integration time of the spectrometer, such that we can compare the reflection from the mirror for short integration times to the data collected from the samples for long integration times. Even at the spectroscope's lowest integration time, the mirror reference would saturate the detector; thus, the light was partially blocked (4% transmission), and this factor (0.04) was

also included in the estimation. The reflectance with respect to a Lambertian scatterer is then given by

$$R = \frac{I_{\text{sample}} - B_{\text{sample}}}{I_{\text{mirror}} - B_{\text{mirror}}} \frac{t_{\text{mirror}} 0.04}{t_{\text{sample}}} \frac{2\pi}{\Omega_c}$$

**Quantifying Reflectance in the Theoretical Model of the Microstructures' Optical Properties.** Spectra for different light incidence and observation conditions were calculated as presented in our previous work.<sup>5</sup> However, absolute values of these spectra were not included in these initial calculations. Here, we have included the reflectance relative to a Lambertian scatterer. In order to do this, we identified the fraction of light hitting the structure's internal interface that undergoes TIR (much of the light strikes the interface at an angle less than the critical angle, as shown in Figure S6, and thus does not contribute to the color generation by TIR and interference). We calculate the area of the interface that accepts incident light into TIR trajectories by determining where light that is striking the internal interface at the critical angle passes through the top plane, as shown in Figure S6. The incoming trajectory of a ray of light can be parameterized by

$$\begin{pmatrix} x \\ y \\ z \end{pmatrix} = \begin{pmatrix} x_i \\ y_i \\ z_i \end{pmatrix} + c \begin{pmatrix} -\sin(\theta_{\text{in}}) \\ 0 \\ \cos(\theta_{\text{in}}) \end{pmatrix} \quad (1)$$

Here,  $(x_i, y_i, z_i)$  is the location on the concave interface, where the incident ray first hits the surface,  $\theta_{\text{in}}$  is the illumination angle measured from the vertical, and  $c$  is a parameter that will be specified below. The origin of the coordinate system lies at the center of curvature of the interface. The normal of the interface at the location of intersection with the incident light ray is  $\frac{1}{R} \begin{pmatrix} x_i \\ y_i \\ z_i \end{pmatrix}$ , such that the local angle of incidence is

$$\cos(\alpha) = -\frac{1}{R} \begin{pmatrix} x_i \\ y_i \\ z_i \end{pmatrix} \cdot \begin{pmatrix} -\sin(\theta_{\text{in}}) \\ 0 \\ \cos(\theta_{\text{in}}) \end{pmatrix} = \frac{x_i \sin(\theta_{\text{in}}) - z_i \cos(\theta_{\text{in}})}{R} \quad (2)$$

We wish to identify the locations  $(x, y, z)$  on the top plane of the structure that correspond to the critical angle  $\alpha_c = \sin^{-1} \frac{n_2}{n_1}$ .

We note that the  $z$  location is set by how deeply embedded the sphere is:  $z = -R \cos \theta_{\text{CA}} = z_i + c \cos(\theta_{\text{in}})$

$$\Rightarrow c = \frac{(R \cos(\theta_{\text{CA}}) - z_i)}{\cos \theta_{\text{in}}} \quad (3)$$

Combining eqs 1–3, we obtain curve  $(x, y)$  parameterized by  $x_i$ :

$$x = x_i - \frac{(R \cos(\theta_{\text{CA}}) - z_i)}{\cos \theta_{\text{in}}} \sin(\theta_{\text{in}})$$

$$y = y_i = \pm \sqrt{R^2 - x_i^2 - z_i^2}$$

where  $z_i = \frac{(R \cos(\alpha_c) + x_i \sin(\theta_{\text{in}}))}{\cos(\theta_{\text{in}})}$ .

This provides the region in a dome that light of incidence angle  $\theta_{\text{in}}$  can strike to undergo TIR. We assume close packing of the spheres and so use a hexagonal unit cell, as shown in Figure S6, to calculate the overall area fraction  $f_{\text{in}}$ . For domes

with contact angle  $\theta_{\text{CA}} = 72^\circ$  with  $n_1 = 1.51$  and  $n_2 = 1.33$ , a total of  $f_{\text{in}} = 10.7\%$  of the incident light will undergo TIR.

The reflectance can then be calculated by

$$R = \frac{I(\theta, \phi)}{\int_0^{2\pi} \int_0^{\pi/2} I(\theta, \phi) \sin(\theta) d\theta d\phi} f_{\text{in}}$$

We assume the reflectance of a Lambertian scatterer to be  $\frac{1}{2\pi}$  relative to the reflectance of a mirror, so the relative reflectance of the dome structure with respect to a Lambertian scatterer is then  $R2\pi$ .

**Code Availability.** The MATLAB code used to implement the optical model and generate simulated color distributions is available for download from <https://github.com/snnagel/Structural-Color-by-Cascading-TIR>.

## ■ ASSOCIATED CONTENT

### Supporting Information

The Supporting Information is available free of charge at <https://pubs.acs.org/doi/10.1021/acsmaterialslett.0c00143>.

Video S1: a polymer dome array displays iridescent structural color (MOV)

Video S2: stretching elastomer films causes changes in structural color (MOV)

Video S3: drawing in structural color using changes in refractive index contrast (MOV)

Video S4: as liquid crystal in PDMS wells is heated to the isotropic state, structural color from TIR changes (MOV)

Additional figures including photographs, optical profilometry, color distributions, reflection spectra, radius of curvature, contact angle, transmission optical micrograph, and a diagram (PDF)

## ■ AUTHOR INFORMATION

### Corresponding Author

Lauren D. Zarzar – Department of Materials Science and Engineering, Department of Chemistry, and Materials Research Institute, The Pennsylvania State University, University Park, Pennsylvania 16802, United States; [orcid.org/0000-0002-3287-3602](https://orcid.org/0000-0002-3287-3602); Email: [ldz4@psu.edu](mailto:ldz4@psu.edu)

### Authors

Amy E. Goodling – Department of Materials Science and Engineering, The Pennsylvania State University, University Park, Pennsylvania 16802, United States

Sara Nagelberg – Department of Mechanical Engineering, Massachusetts Institute of Technology, Cambridge, Massachusetts 02139, United States

Mathias Kolle – Department of Mechanical Engineering, Massachusetts Institute of Technology, Cambridge, Massachusetts 02139, United States

Complete contact information is available at: <https://pubs.acs.org/doi/10.1021/acsmaterialslett.0c00143>

### Notes

The authors declare the following competing financial interest(s): A provisional patent was filed relating to this work.

## ■ ACKNOWLEDGMENTS

L.D.Z. and A.E.G. acknowledge support from the Department of Chemistry, the Department of Materials Science and

Engineering, and the Materials Research Institute at The Pennsylvania State University. S.N. and M.K. were supported in part by the U. S. Army Research Office through the Institute for Soldier Nanotechnologies at MIT, under Contract W911NF-13-D-0001. A.E.G., S.N., M.K., and L.D.Z. gratefully acknowledge support from the National Science Foundation's CBET program "Particulate and Multiphase Processes" under Grants 1804241 and 1804092.

## ■ REFERENCES

- (1) Kuhn, H. A Quantum-mechanical Theory of Light Absorption of Organic Dyes and Similar Compounds. *J. Chem. Phys.* **1949**, *17*, 1198–1212.
- (2) Kinoshita, S.; Yoshioka, S.; Miyazaki, J. Physics of Structural Colors. *Rep. Prog. Phys.* **2008**, *71*, 076401.
- (3) Fu, Y.; Tippets, C. A.; Donev, E. U.; Lopez, R. Structural Colors: From Natural to Artificial Systems. *Wiley Interdiscip. Rev. Nanomedicine Nanobiotechnology* **2016**, *8*, 758–775.
- (4) Sun, J.; Bhushan, B.; Tong, J. Structural Coloration in Nature. *RSC Adv.* **2013**, *3*, 14862–14889.
- (5) Goodling, A. E.; Nagelberg, S.; Kaehr, B.; Meredith, C. H.; Cheon, S. I.; Saunders, A. P.; Kolle, M.; Zarzar, L. D. Colouration by Total Internal Reflection and Interference at Microscale Concave Interfaces. *Nature* **2019**, *566*, 523–527.
- (6) Kinoshita, S. *Structural Colors in the Realm of Nature*; World Scientific, 2008.
- (7) Kinoshita, S.; Yoshioka, S. Structural Colors in Nature: The Role of Regularity and Irregularity in the Structure. *ChemPhysChem* **2005**, *6*, 1442–1459.
- (8) Xia, Y.; Whitesides, G. M. Soft Lithography. *Annu. Rev. Mater. Sci.* **1998**, *28*, 153–184.
- (9) Zhao, Y.; Xie, Z.; Gu, H.; Zhu, C.; Gu, Z. Bio-Inspired Variable Structural Color Materials. *Chem. Soc. Rev.* **2012**, *41*, 3297–3317.
- (10) Aguirre, C. I.; Reguera, E.; Stein, A. Tunable Colors in Opals and Inverse Opal Photonic Crystals. *Adv. Funct. Mater.* **2010**, *20*, 2565–2578.
- (11) Isapour, G.; Lattuada, M. Bioinspired Stimuli-Responsive Color-Changing Systems. *Adv. Mater.* **2018**, *30*, 1707069.
- (12) Sandt, J. D.; et al. Stretchable Optomechanical Fiber Sensors for Pressure Determination in Compressive Medical Textiles. *Adv. Healthcare Mater.* **2018**, *7*, 1800293.
- (13) De Coninck, J.; De Ruijter, M. J.; Voué, M. Dynamics of Wetting. *Curr. Opin. Colloid Interface Sci.* **2001**, *6*, 49–53.
- (14) Chen, L.; Bonaccorso, E. Effects of Surface Wettability and Liquid Viscosity on the Dynamic Wetting of Individual Drops. *Phys. Rev. E - Stat. Nonlinear, Soft Matter Phys.* **2014**, *90*, 022401.
- (15) Jenkins, F. A.; White, H. E. *Fundamentals of Optics*; McGraw-Hill, 2001.
- (16) Singh, S.; Dunmur, P. D. A. *Liquid Crystals Fundamentals*; World Scientific: Farrer Road, Singapore, 2002.
- (17) Zheng, W. J.; Huang, M. H. Use of Polydimethylsiloxane Thin Film as Vertical Liquid Crystal Alignment Layer. *Thin Solid Films* **2012**, *520*, 2841–2845.
- (18) Li, J.; Gauza, S.; Wu, S. T. Temperature Effect on Liquid Crystal Refractive Indices. *J. Appl. Phys.* **2004**, *96*, 19–24.
- (19) Ahn, S. K.; Kasi, R. M.; Kim, S. C.; Sharma, N.; Zhou, Y. Stimuli-Responsive Polymer Gels. *Soft Matter* **2008**, *4*, 1151–1157.
- (20) Hu, J.; Zhang, G.; Liu, S. Enzyme-Responsive Polymeric Assemblies, Nanoparticles and Hydrogels. *Chem. Soc. Rev.* **2012**, *41*, 5933–5949.
- (21) Ulijn, R. V. Enzyme-Responsive Materials: A New Class of Smart Biomaterials. *J. Mater. Chem.* **2006**, *16*, 2217–2225.
- (22) Hu, J.; Liu, S. Responsive Polymers for Detection and Sensing Applications: Current Status and Future Developments. *Macromolecules* **2010**, *43*, 8315–8330.